

The Uranian Geometric Albedo: An Analysis of Atmospheric Scatterers in the Near-Infrared

Charles M. Walter and Mark S. Marley

Department of Astronomy, Box 30001/Department 4500, New Mexico State University, Las Cruces, New Mexico 88003
E-mail: mmarley@nmsu.edu

Received August 7, 1997; revised December 15, 1997

Narrowband images of Uranus in the near-infrared from Apache Point Observatory were employed to derive the globally averaged properties of scatterers in the atmosphere in the post-Voyager epoch. In order to best probe different levels of the stratosphere and upper troposphere we measured and modeled the planetary geometric albedo using seven filters ranging from 1.28 to 2.36 μm . Since 1986 there has been a 20-fold increase in the stratospheric haze-column density, while the tropospheric cloud characteristics have remained largely the same. Our results suggest an upper limit on the optical thickness of the lower H_2S cloud of 15 at 1.58 μm . © 1998 Academic Press

Key Words: abundances, atmospheres; atmospheres, composition; atmospheres, structure; clouds; Uranus, atmosphere.

1. INTRODUCTION

Since the 1970s it has been recognized that several scattering layers in the uranian atmosphere were required to explain the planet's spectrum. Binder and McCarthy (1972) postulated the existence of a CH_4 condensate layer, and Savage and Caldwell (1974) showed that high-altitude hazes could be used to explain an ultraviolet albedo lower than that predicted of a clear Rayleigh-scattering atmosphere. The required scattering layers are located higher in the atmosphere than the optically thick cloud deck typically used to define the bottom of the visible atmosphere. Current atmospheric models are largely based upon data taken in the next decade, both from ground-based observatories and the Voyager 2 flyby in 1985/1986. Pollack *et al.* (1987) used the Voyager high phase angle imaging along with microphysical coagulation models to constrain the profile of stratospheric hazes and placed limits on the size of the CH_4 ice particles. Baines *et al.* (1995a) analyzed the H_2 quadrupole and CH_4 absorption features measured by ground-based spectroscopy in the red to constrain the tropospheric CH_4 mixing ratio.

Prior to 1994, Uranus presented a featureless disk to ground-based observers, but this has changed in the in-

tervening years. Hubble Space Telescope Observations of Uranus on August 14, 1994 show a bright cloud covering the south polar region (Zellner *et al.* 1994). This feature was seen in subsequent ground-based observations (Baines *et al.* 1995b, Walter and Marley 1995), and by another HST program on July 3, 1995 (Walter *et al.* 1997).

Uranus is unique among the planets of our Solar System in that its rotation axis is inclined 98° to the ecliptic, resulting in essentially 42 consecutive years of continuous sunlight alternating on each hemisphere. The haze material is thought to largely consist of hydrocarbons created by UV photolysis of CH_4 (Atreya *et al.* 1991). The increased sunlight being received at the south pole due to the summer solstice of 1986 should have resulted in an increase in the column density of haze particles. Disk-averaged brightness changes in Uranus are documented to have previously occurred. Lockwood *et al.* (1983) found a 14% increase in the visual albedo between 1963 near-equatorial observations and 1981 observations at a sub-earth latitude of -68° .

All these results have been derived from observations of the planet in the visible, but by observing in the near-infrared beyond 1 μm we can improve upon current atmosphere models in two distinct areas. The grains that make up the tropospheric cloud are thought to be on the order of 1 μm (Rages *et al.* 1991) in size, giving a scattering size parameter ($x = 2\pi r/\lambda$) ranging from 2 to 7 over the 1–2.5- μm regime. The scattering efficiency Q_{set} varies substantially over these size parameters. Mie theory can thus constrain the mean particle size. In addition, the molecular gaseous absorption bands of CH_4 and H_2 are stronger in the near-IR. This allows greater sensitivity to the properties of the stratosphere.

Here we report on observations aimed at achieving a better understanding of the overall properties of scatterers in the uranian atmosphere and their temporal variation. We measured the planetary geometric albedo using several narrowband filters in the near-IR and then used this data as the primary constraint for a new atmospheric model. This is the first attempt to use near-IR data to examine

TABLE I
Observations

Filter	August 12, 1995	June 5, 1996	October 30, 1996
1.28 μm			60
1.58 μm	360	150	
1.70 μm		125	
1.99 μm		600	
2.12 μm			600
2.25 μm		700	
2.36 μm		220	210
FWHM	1.7"	1.7"	1.5"
Phase angle	1.0°	2.2°	2.8°
Planet airmass	1.7	1.6–1.7	2.3–3.0
Star airmass	1.4	1.4–1.5	2.1–2.3

Note. Total exposure time is given in seconds. A blank space indicates that no observation was made.

the atmospheric properties since the work of Fink and Larson (1979), who examined a planetary spectrum with a spectral resolution of 3.6 cm^{-1} . They found that the extinction in these bands from gaseous absorption is so high that Rayleigh scattering is still an important source of scattered photons even as far in the infrared as $1.5 \mu\text{m}$. By choosing our filters to cover varying intensities of H_2 and CH_4 absorption bands as well as continuum wavelengths, we were able to probe effectively the stratosphere and upper troposphere of the atmosphere to derive our model. In Section 2 we describe our observations and the photometric techniques used in our albedo measurements. We present our model and the representation of the various atmospheric constituents in Section 3. Our results are given in Section 4, and finally, Section 5 discusses their implications.

2. OBSERVATIONS

The data presented here were acquired using the Astrophysical Research Consortium 3.5-m telescope at Apache Point Observatory in Sunspot, NM. Using the GRIM II HgCdTe 256×256 array, which is sensitive from 1.0 to $2.5 \mu\text{m}$, we observed Uranus and the near-IR standard star *G*811.1 (Elias *et al.* 1982). The dates of observation, phase angles, filters used, total integration times, and median seeing FWHM are given in Table I. In f/10 mode, the plate scale is $0.236''/\text{pix}$, meaning Uranus typically subtends a diameter of 15 pixels, with a FWHM resolution disk 7 pixels in diameter. Data were sky and dark-subtracted, flat-fielded, and corrected for the nonlinearity of the camera. Multiple exposures in each filter were coadded. Bad pixels and cosmic ray hits were corrected for by nearest-neighbor interpolation. Continuum images from all 3 dates are shown in Fig. 1.

The geometric albedo of a planet is defined as that fraction of the incoming sunlight that is scattered back to Earth at 0° phase angle (opposition) relative to that scattered by a nonabsorbing Lambert disk. Because our observations were taken near opposition, with phase angles $<3^\circ$, no correction for the phase angle was used. The solar spectrum at 1 AU is given in the tables of Labs and Neckel (1968). This radiation is attenuated upon reaching Uranus by a factor $H_\oplus^2 H_U^{-2}$, where H_\oplus and H_U are the mean Earth heliocentric distance, 1 AU, and the heliocentric distance of Uranus at the time of observation, respectively. This light is further attenuated upon scattering from the planet's atmosphere and its subsequent arrival at Earth by a factor $A R_U^2 G_U^{-2}$, where A is the geometric albedo, R_U is the radius of Uranus, and G_U is the geocentric Uranian distance, so the resultant wavelength dependent geometric albedo can be determined from

$$A = \left(\frac{H_U G_U}{H_\oplus R_U} \right)^2 \frac{DN_U}{DN_\odot}, \quad (1)$$

where DN_U and DN_\odot are the digital counts of photons detected from Uranus and the Sun.

2.1. Photometry

To find DN for the sun we multiplied the stellar standard's DN by the ratio between the known solar flux (Labs and Neckel 1968) and the standard star, for which broadband H and K fluxes were available as well as a CO and H_2O index, to account for the stellar absorption by these molecules at narrowband filters similar to our own at 2.36 and $1.99 \mu\text{m}$ (Elias *et al.* 1982). For the other narrowband filters we linearly interpolated the star's magnitude using the broadband values.

The initial flux we measured includes contributions from the planetary disc as well as the smeared ring system. Photometric errors in this value can be determined by knowing the errors inherent in the observations of Uranus and the standard star, while neglecting the errors in the knowledge of the distance and radius of Uranus, which are comparatively well established. The radius used was 25450 km , which is recommended by the International Astronomical Union (Davies *et al.* 1995). While our observations probe a slightly lower pressure than the 1-bar level used to determine this radius, use of this radius is necessary for comparison with other works.

The error ΔDN_U is determined by adding in quadrature the Poissonian noise with the uncertainty in measurement. For ΔDN_* , the Poissonian noise is replaced by the known flux uncertainty of the standard, 0.015 mag (Elias *et al.* 1982). The observations of October 30, 1996 were hindered by a variable sky level, so it was necessary to calibrate the planetary observations using the known moon reflectances.

TABLE II
Geometric Albedos

Filter	Initial albedo	Corrected albedo
August 12, 1995		
1.58 μm	$(9.3 \pm 0.4) \times 10^{-2}$	$(9.3 \pm 0.4) \times 10^{-2}$
June 5, 1996		
1.58 μm	$(8.8 \pm 0.2) \times 10^{-2}$	$(8.8 \pm 0.2) \times 10^{-2}$
1.70 μm	$(1.09 \pm 0.03) \times 10^{-3}$	$(8.1 \pm 0.5) \times 10^{-4}$
1.99 μm	$(1.6 \pm 0.03) \times 10^{-3}$	$(1.3 \pm 0.1) \times 10^{-3}$
2.25 μm	$(4.5 \pm 0.2) \times 10^{-4}$	$(1.6 \pm 0.4) \times 10^{-4}$
2.36 μm	$(5.7 \pm 0.4) \times 10^{-4}$	$(2.8 \pm 0.6) \times 10^{-4}$
October 30, 1996		
1.28 μm	$(9.4 \pm 1.3) \times 10^{-2}$	$(9.4 \pm 1.3) \times 10^{-2}$
2.12 μm	$(6.0 \pm 0.8) \times 10^{-4}$	$(3.0 \pm 0.9) \times 10^{-4}$
2.36 μm	$(4.2 \pm 0.9) \times 10^{-4}$	$(1.2 \pm 0.9) \times 10^{-4}$

We compared broadband K images of the moon Ariel taken on June 5, 1996 in photometric conditions with those taken in the October run. Ariel was the only moon that was present in both images and had published reflectances over the entire wavelength range (Brown 1983, Brown and Cruikshank 1983). For this data, Ariel then replaces the standard with a three-component error, the reflectance error of 10% along with the photometric errors in both observations. Resultant pre-ring-subtraction albedos and errors are listed in Table II. Other photometric uncertainties less than 2% include the uncertainty in the extinction curve, nonlinearity correction, the published solar fluxes, and timing errors for short exposures. The variation of the moon's reflectivity from opposition to the phase angles observed in this work can in extreme cases be as much as half a magnitude (Veverka *et al.* 1986). For the 2.12- and 2.36- μm bandpasses, the effect on the results is less significant due to the already high errors in photometry and modeling, but it remains an additional source of error for the 1.28- μm data.

We chose seven filters that were available with the GRIM II instrument, narrowband filters centered at 1.28, 1.58, 1.70, 1.99, 2.12, 2.25, and 2.36 μm . Transmission curves at room temperature and at the detector operation temperature of 77 K were available for all filters except the 1.99-

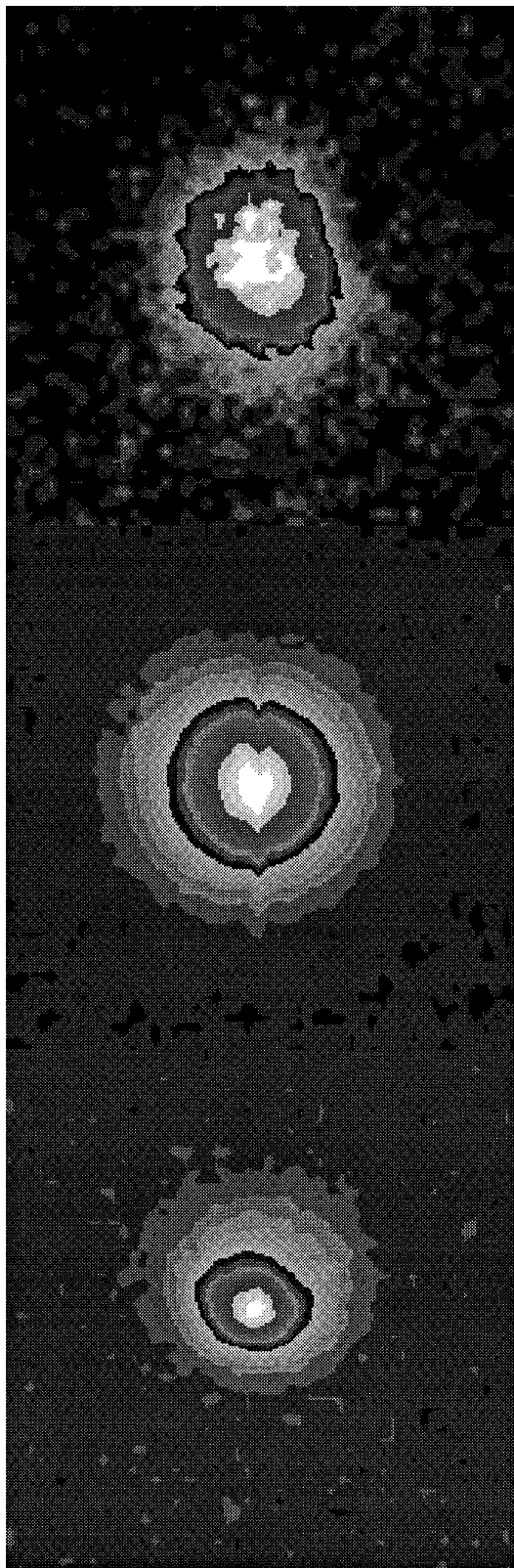


FIG. 1. Observations of Uranus at three recent epochs by the ARC 3.5-m telescope displayed as filled contour maps. In the bottom panel is an H-band image taken on August 12, 1995, showing asymmetry in brightness in the south polar region. The middle panel is an image with the same filter taken on June 6, 1996, showing a smooth disk. On the top a narrowband 1.28- μm filter image of the planet on October 30, 1996, again showing a smooth disk. The images are rotated so that north is on top.

TABLE III
Filter Characteristics

Name	Center (μm)	FWHM (μm)
Pa β	1.2823	0.0146
Narrow continuum	1.580	0.010
Methane	1.700	0.050
Steam	1.99	0.02
H ₂ $\nu = 1 \rightarrow 0$ S(1)	2.122	0.028
H ₂ $\nu = 2 \rightarrow 1$ S(1)	2.2485	0.0239
CO band	2.36	0.09

μm filter, which has identical values to the 1.58- μm filter but stretched to fit the greater FWHM. The filter centers and FWHM are given in Table III.

2.2. Ring Subtraction

For filters in which the planet is dark (typically those with albedos less than 10^{-3}), smearing of the planetary disc with the ring system due to the large PSF created a significant source of error and prevented direct removal of the rings. The ring contribution was modeled using the derived effective ring location, radius, and albedo of Nicholson and Jones (1980) scaled to the appropriate geometry. The ring system projects an ellipse upon the sky depending upon the sub-Earth latitude θ at the time of observation, where a is the semimajor axis along the uranian equatorial plane, and $b = a \sin \theta$. Then the effective cross-sectional area S is $\pi \sin \theta (a_2^2 - a_1^2)$, where a_2 and a_1 are the Nicholson and Jones' effective ring-edge radial distances determined by the effective width. An effective spherical radius can then be determined as $R_{\text{eff}} = \sqrt{S/\pi} = \sqrt{\sin \theta (a_2^2 - a_1^2)}$. The contribution from the ring can then be determined using

$$A_r = a_r \left(\frac{R_{\text{eff}}}{R_U} \right)^2 = 4.03 \times 10^{-4} \sin |\theta|, \quad (2)$$

where A_r is the contribution to the total albedo from the rings, and a_r is the ring albedo, a constant within 5% over the range 2.1–2.5 μm . This approach has one dominant source of error, the ring albedo for which we use $3.0 \pm 0.4 \times 10^{-2}$. The albedo correction for each night and corrected albedo values are given in Tables II and IV.

TABLE IV
Ring Corrections

Date	θ	Albedo correction
August 12, 1995	-51.0	$3.14 \pm 0.44 \times 10^{-4}$
June 5, 1996	-44.6	$2.83 \pm 0.40 \times 10^{-4}$
October 30, 1996	-47.9	$2.99 \pm 0.42 \times 10^{-4}$

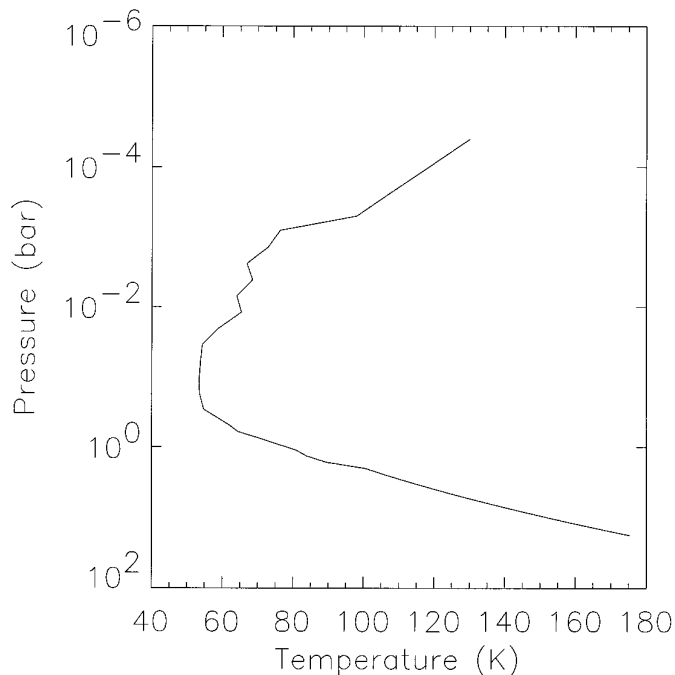


FIG. 2. The pressure–temperature profile used by the model. Data is taken from the Voyager 2 RSS experiment results (Lindal *et al.* 1987).

3. MODEL

Our geometric albedo model is based upon the model of McKay *et al.* (1989), which uses the Eddington source method of Toon *et al.* (1989) to compute the upward and downward monochromatic fluxes through 35 plane-parallel layers spaced approximately evenly in $\log P$, where P is pressure. This technique is useful as it allows for rapid flux computation, and the flux errors of this approximation do not exceed 11% (Toon *et al.* 1989), which is typically more accurate than our knowledge of gaseous absorption coefficients and the photometry. In this model, we examine the effects of six opacity sources—Rayleigh scattering, scattering and absorption from stratospheric hazes, two tropospheric clouds, and H₂ and CH₄ gas absorption. The temperature profile is that derived from the Voyager 2 RSS experiment (Lindal *et al.* 1987), shown in Fig. 2. In Table V we list the free parameters explored in the analysis.

TABLE V
Free Parameters

n_i	Haze imaginary index of refraction
f_{hze}	Haze column density scaling factor
$f_{\text{CH}_4, \text{s}}$	Stratospheric CH ₄ mixing ratio
P_{eld}	Pressure of CH ₄ cloudtop
τ_{eld}	Optical depth of CH ₄ cloud
τ_{eld2}	Optical depth of lower cloud
$\tilde{\omega}_{\text{eld2}}$	Single-scattering albedo of lower cloud

TABLE VI
Haze Constituents^a

Pressure		Real index of refraction	Substance
Top (bar)	Bottom (bar)		
0	2.4×10^{-3}	1.42	C_4H_2
2.4×10^{-3}	12×10^{-3}	1.33	C_2H_2
12×10^{-3}		1.44	C_2H_6

^a From the model of Rages *et al.* (1991).

3.1. Scatterers

3.1.1. Rayleigh scattering. Rayleigh scattering is treated as in Hansen and Travis (1974) and Raman scattering as in Rages *et al.* (1991) and is not allowed to increase the single-scattering albedo of any layer above 1. Contributions of the dominant constituents, H_2 , He, and CH_4 gas are used, with the refractive index given in the tables of Allen (1973).

3.1.2. Stratospheric haze. Direct evidence for hazes in the stratosphere was first seen in high phase angle Voyager

images (Pollack *et al.* 1987). The subsequent analysis by Rages *et al.* (1991) yielded a multilayer profile with the number densities, mean modal radius, and size distribution as a function of pressure. We interpolated these values to our own grid and used this model as a baseline. Because the haze is thought to consist of higher order hydrocarbons resulting from solar UV photolysis of CH_4 photons high in the atmosphere (Pollack *et al.* 1987), we represented the real index of refraction of the haze in each level as that of the expected dominant source, as shown in Table VI. The haze particles were modeled as spherical Mie scatterers, with the mean particle size and column densities scaled in efforts to fit the observations. Because high values of the imaginary index of refraction ($n_i > 10^{-2}$) gave albedos grossly inconsistent with the observations, we adopted a value of 5×10^{-3} .

3.1.3. CH_4 cloud. Prinn and Lewis (1973) demonstrated that there could be a thin cloud layer at 1 bar by fitting the geometric albedo in the visible and near-infrared. By comparing the spectral observations in bands both sensitive and insensitive to CH_4 , Baines (1983) and Baines and Bergstrahl (1986) showed that there was an order of magnitude more haze than could be accounted for in the sensitive bands, confirming the existence of a 1-bar tropospheric optically significant cloud. By analysis of the bifurcation of the RSS radio signal, Lindal *et al.* (1987) deter-

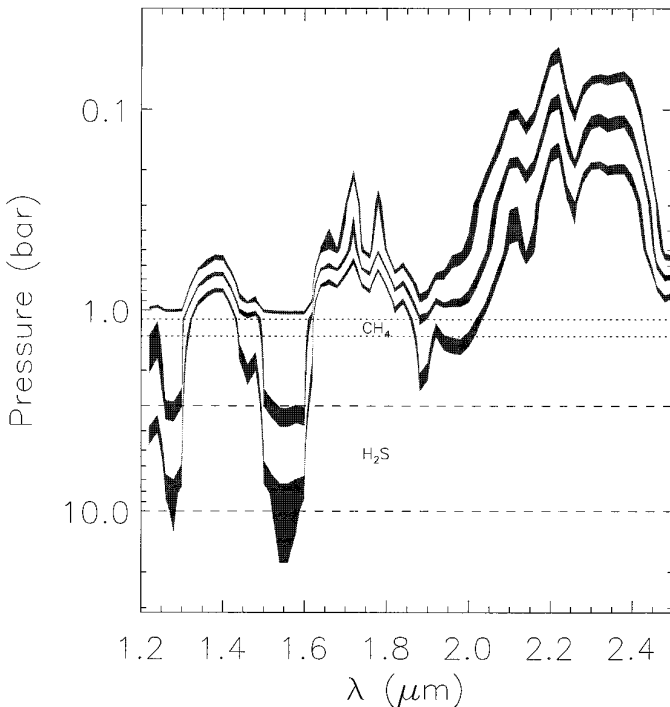


FIG. 3. Optical depth is illustrated as a function of wavelength and pressure. From the top, the three lines represent where in the atmosphere incoming radiation encounters extinction optical depths of 1, 3, and 9. Line widths represent a $\pm 15\%$ model error. The locations of the two tropospheric clouds as used in our model are indicated. Total optical thickness is computed from molecular absorption by H_2 and CH_4 , stratospheric hazes, tropospheric clouds, and Rayleigh scattering.

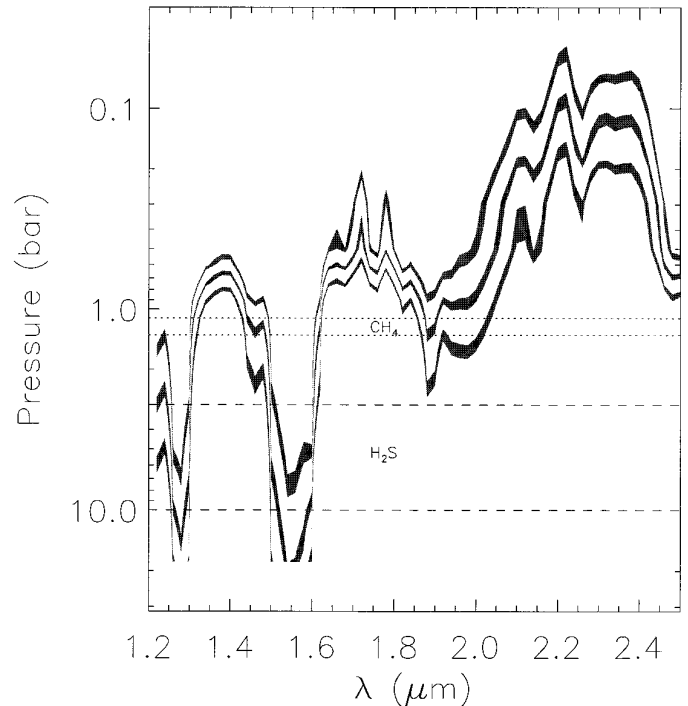


FIG. 4. Similar to Fig. 3, but using only the contributions from molecular absorption by H_2 and CH_4 . The difference is only noticeable in the continuum regions probed by our 1.28- and 1.58- μm filters.

mined the CH₄ cloud top to be at 1.2 bar. We modeled this cloud using Mie theory for 1- μm radius CH₄ spherical particles. Although this value is poorly constrained, it contributes very little to the model error unless the true value is drastically smaller. This is because the total optical thickness is a free parameter, and particles of this size or greater are largely forward-scattering and nearly conservatively scattering at these wavelengths in the absence of impurities in the cloud.

Although the formation mechanisms of the stratospheric and CH₄ hazes are different, for the CH₄ we used a log-normal size distribution equal to that in the lower levels of the stratospheric haze. The optical properties were taken from Pearl *et al.* (1991) for Phase I CH₄ at 30 K. Further constraints on the absorptive characteristics of this cloud were prevented by the atmosphere being optically thick at the level of the cloud at those wavelengths where CH₄ is absorbing (see Fig. 3). We examined the effects of moving the cloud top higher in the troposphere and varying the number density of particles by scaling the total optical extinction.

3.1.4. Lower cloud. Thermochemical arguments suggest that the lower cloud consists of H₂S ice. NH₃ condenses out near 10 bars (Weidenschilling and Lewis 1973), with a lower cloud consisting of NH₄SH. NH₃ is severely depleted in the lower troposphere (Gulkis *et al.* 1983), while the models of de Pater *et al.* (1991) show that H₂S is enriched by two orders of magnitude over solar abundance.

Herzberg (1952) analyzed the properties of molecular hydrogen in an effort to explain the results of Kuiper (1949), who measured an absorption feature at 0.83 μm , the location of the H₂ 3–0 quadrupole. In his study, Herzberg calculated that the visible atmosphere consisted of 2 bars of H₂. Follow-up work involved the calculation of the equivalent width of the feature (Encrenaz and Owen 1973, Trafton 1976, Smith *et al.* 1980). By analyzing the observations of Trauger and Bergstralh (1981), Baines and Bergstralh (1986) were able to constrain the location of the lower cloudtop to between 2.4 and 3.2 bar. A later reanalysis using improved laboratory data changed the allowable region to be between 2.9 and 4.2 bar (Baines *et al.* 1995a).

Because of the uncertainties involved in higher atmospheric features, the scattering properties of this cloud were not well defined, so we took as free parameters the scattering asymmetry factor $\langle \cos \Theta \rangle$, the single-scattering albedo $\tilde{\omega}$, the column density of particles, and the pressure top of this cloud. The cloud was initially modeled as homogeneous and lying between 3 and 10 bar, with the optical depth in each layer proportional to the pressure difference in that layer.

Molecular Absorption

3.2.1. H₂. Conrath *et al.* (1987) determined the helium mole fraction in the upper troposphere to be 0.152 ± 0.033 ,

which we take to be constant throughout the entire model. With CH₄ being the only other significant constituent, the rest of the atmosphere is modeled as H₂. The rotovibrational fundamental and first overtone of H₂ are located within our spectral region. We computed the absorption coefficients using codes provided by A. Borysow (Borysow 1991, Borysow 1992, Borysow and Frommhold 1989, Borysow *et al.* 1989, Zheng and Borysow 1995, Birnbaum *et al.* 1996) for H₂–H₂ and H₂–He collisions over our temperature range. These codes assume an equilibrium ortho to para hydrogen ratio, consistent with the previous observations (Hanel *et al.* 1986, Baines *et al.* 1995a).

3.2.2. CH₄. Methane absorption longward of 1.6 μm was treated by weighting the exponential sum absorption coefficients from the Baines *et al.* (1993) quasi-random narrow band model by their Gauss weights. They derived coefficients over a large pressure grid at three temperatures, 112, 188, and 295 K. Because the near-IR behavior of methane is not well established at low temperatures, we use the low temperature (112 K) values for all stratospheric and upper-tropospheric layers and interpolate between the 112 and 188 K values otherwise. All values are interpolated on pressure and wavenumber grids, with resolution of 0.25 in $\log P$ and 10 cm^{-1} in wavenumber. Shortward of 1.6 μm we used the low temperature (190 K) CH₄ absorption coefficients of Strong *et al.* (1993). These molecular band models were fitted to a Goody–Voigt random band model with a spectral resolution of 0.25 cm^{-1} , but are not pressure dependent.

The mixing ratio of CH₄ in the stratosphere is highly uncertain, and only upper limits can be set, assuming the fraction does not exceed that measured at the tropopause by Voyager. The tropopause saturation mixing ratio is 10^{-4} , however the RSS results show the equatorial mixing ratio to be only 30% of saturation. From spectral observation near the ν_4 fundamental band, Orton *et al.* (1987) set an upper limit on the disk-averaged stratospheric mixing ratio of 10^{-5} . Below the tropopause the Clausius–Clapeyron equation is followed assuming saturation until it reaches the observed tropospheric ratio of 2.3% derived from RSS results (Lindal *et al.* 1987). This equation relates the vapor pressure of a substance to the temperature and is of the form

$$\ln P = -\frac{\Delta H_{\text{vap}}}{RT} + C, \quad (3)$$

where ΔH_{vap} is the molar heat of evaporation (9.2 kJ mol^{-1}) for CH₄, R is the gas constant (8.314 $\text{J K}^{-1} \text{mol}^{-1}$), and C is a constant.

4. RESULTS

By obtaining albedo measurements in six separate filters, we sounded various levels of the atmosphere. Figure 3

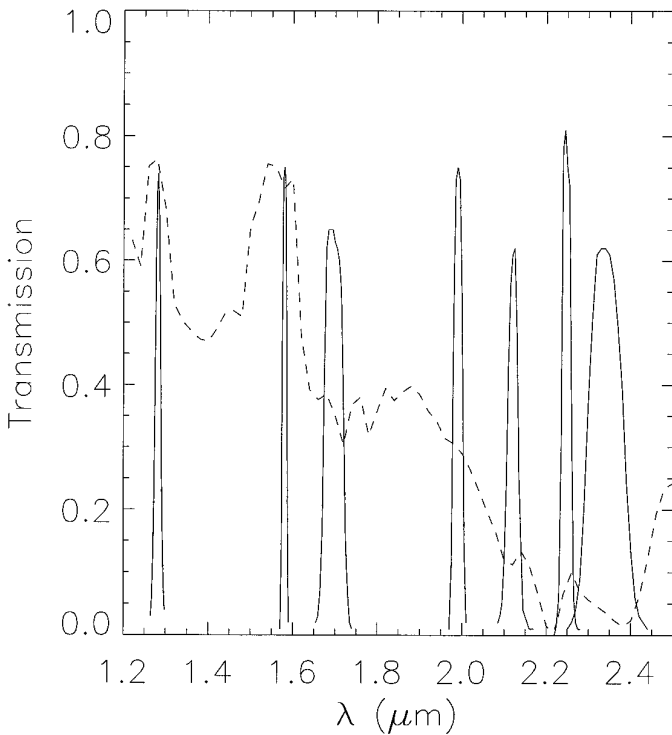


FIG. 5. The transmission characteristics of the seven narrowband filters used in the study centered at 1.28, 1.58, 1.70, 1.99, 2.12, 2.25, and 2.36 μm . The albedo spectrum of our best model is displayed logarithmically for comparison.

illustrates the effective extinction level of the atmosphere as a function of wavelength. Our nominal model shows the level where monochromatic extinction reaches optical depths of 1, 3, and 9. By choosing appropriate filters, various atmospheric levels can be probed. The light eventually seen takes contributions from all manner of scatterers. However, in the deepest molecular absorption bands, enough extinction has taken place so that contributions from the tropospheric clouds are negligible. In Fig. 4, the extinction levels are computed for a clear atmosphere consisting only of gas. Beyond 2 μm , our model is completely insensitive to the tropospheric scatterers.

To model the data, we integrated the model results over each filter bandpass. A weighted average of 9 to 20 monochromatic points was used to determine the final result. Weights were chosen by using the average value of the effective transmission in each region. In Fig. 5, the transmission of each filter is overlain with the best model albedo for comparison.

The filters can be broken up into three groups according to which region of the atmosphere they probe most effectively, the stratosphere group, the CH_4 cloud group, and the troposphere group. Figures 6–11 show the results using the albedos derived in each bandpass, obtained by varying

the available relevant parameters for each band to compute the acceptable solution space. These results are contoured so that every possible value within the combined photometric errors (see Table II) and the radiative transfer code errors (which vary from 12% at continuum wavelengths to 40% in deep H_2 and CH_4 bands) is shaded. Only data from 1996 are used in constraining the best-fit model.

4.1. Stratosphere

Since the near-infrared part of the electromagnetic spectrum is not home to any strong rovibrational fundamentals, it is very unlikely that any haze constituent has a large imaginary index of refraction in the spectral regime covered by this work. Models with n_i less than about 1×10^{-2} were indistinguishable from conservatively scattering particles because the scattering efficiency Q_{scat} is nearly insensitive to n_i in this region, whereas the absorption is insignificant. This model is then not sensitive to the optical characteristics of the haze for values of n_i less than 10^{-2} . To account for this we chose a value for n_i of 5×10^{-3} .

It is difficult to determine the number of haze particles unless their sizes are known and vice versa. An increase in mean particle size would mimic the effect of more haze, and a decrease could be interpreted as a lower column density. To test the likely effect of different particle sizes, we computed the optical depth τ for a conservative Mie scatterer with various particle sizes (Fig. 12). The total transmission $e^{-\tau}$ falls off essentially as λ^{-1} in this spectral range. Decreasing the mean particle size by a factor of 10 results in a decrease in scattering efficiency of five orders of magnitude. Because we could not distinguish between the two effects, we maintained the Rages *et al.* (1991) particle size distribution and adjusted the number of scatterers by using a scaling factor f_{haze} to the column density.

Three program filters overlay bands that are sensitive to CH_4 absorption, 1.70, 2.25, and 2.36 μm . We used the June 5, 1996 albedo for the 1.70- and 2.25- μm results. For 2.36 μm , an average of the June and October 1996 observations weighted by their signal to noise ratios was used. Although the 2.12- μm filter bandpass is not sensitive to CH_4 , it is located at the H_2 $\nu = 1 \rightarrow 0$ S(1) transition, and as such becomes optically thick in the stratosphere. The results derived from the 2.12-, 2.25-, and 2.36- μm filters are internally consistent, but are slightly different than the 1.70- μm result, which sets an upper limit on the haze scaling factor of about 2. Given the uncertainties in CH_4 absorption coefficients at the low stratospheric temperatures, this disagreement is not surprising, so the 1.70- μm result was discarded in favor of the >2 - μm results. The individual parameter spaces for the 2.25- and 2.36- μm filters are shown in Figs. 6 and 7 and are combined with the 2.12- μm result, which is represented as a box in Fig. 8. The allowed values for the haze-scaling factor (where all three

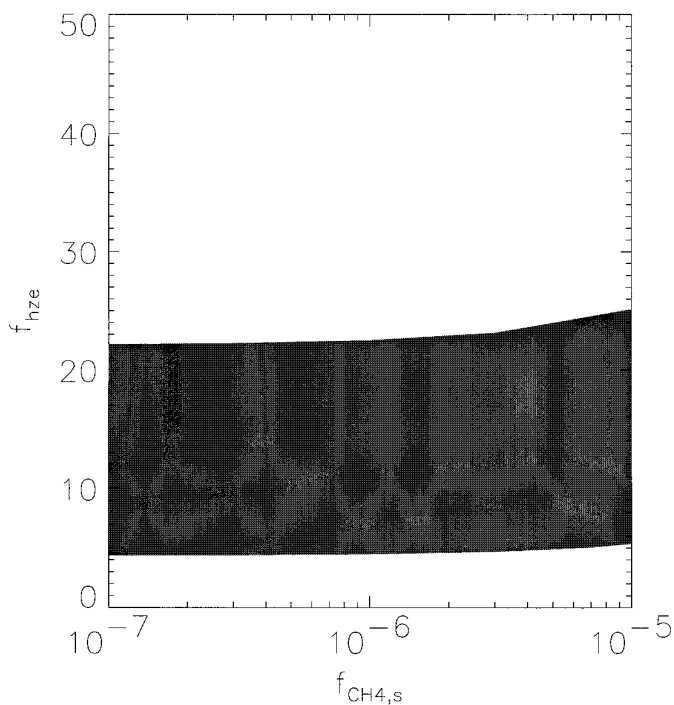


FIG. 6. The solution space for the 2.25- μm results. The shaded regions represent the combination of parameters for the stratospheric CH_4 mixing ratio $f_{\text{CH}_4,\text{s}}$ and haze-scaling factor f_{hze} that produce a geometric albedo within the model and photometric errors.

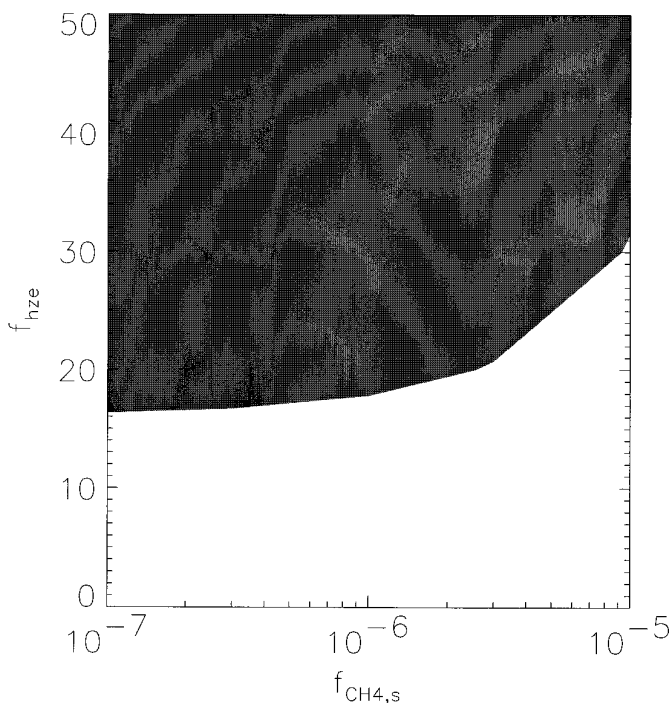


FIG. 7. Similar to Fig. 6 for the 2.36- μm results.

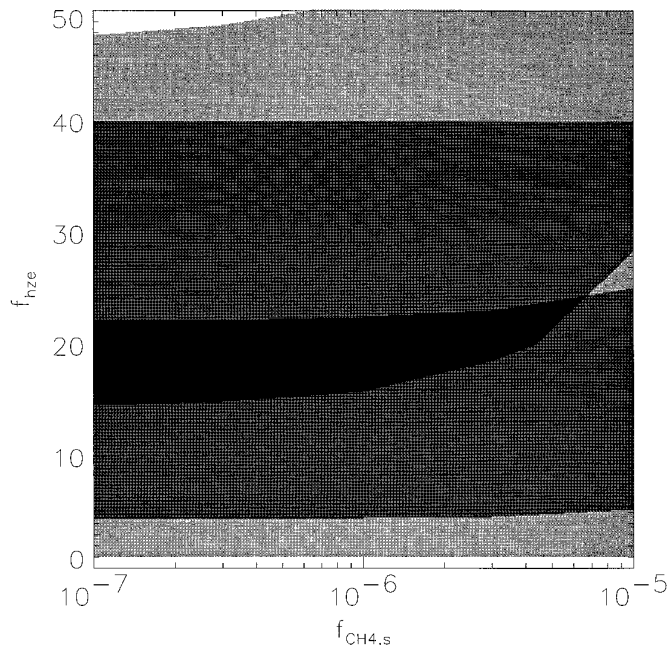


FIG. 8. The solution space for the albedo model code results for three filters at 2.12, 2.25, and 2.36 μm as a function of the haze-column density scaling factor f_{hze} and the stratospheric CH_4 mixing ratio $f_{\text{CH}_4,\text{s}}$. Darker shading represents the overlap of more allowed solutions, with the region bounding haze-scaling factors of 15 and 25 representing an acceptable solution from the results of all three filters.

solution spaces overlap) range from 15 to 25, with a best fit of 20, again using a signal to noise weighting scheme for the three filters. Our results are relatively insensitive to the stratospheric CH_4 mixing ratio.

4.2. CH_4 Cloud

As seen in Fig. 3, the 1.99- μm filter probes to the depth of the CH_4 cloud, but no further. It is possibly the most useful filter, as it is sensitive to the haze-column density, the total extinction optical depth of the cloud, and its vertical location. For small values of the haze-scaling factor, the cloud is the dominant source of extinction, but its importance decreases for the high-scaling factor values determined from our stratospheric modeling. As the cloud moves higher, the necessary column density required to produce the observed albedo decreases, as seen in Fig. 9. Using the haze-scaling factor of 20, the lower limit for the cloudtop is at 0.8 bar, but our best result comes from placing the cloudtop at 1.1 bar, near that found by Voyager (1.2 bar). Use of this bandpass again sets an upper limit on the amount of haze present. The last box in Fig. 9 shows that a haze-scaling factor of 40 yields an albedo higher than our observational upper limit. For large (>15) values of f_{hze} the cloud optical depth is not a large contributor to the back-scattered light, explaining the lack of an asymmetry seen in the images.

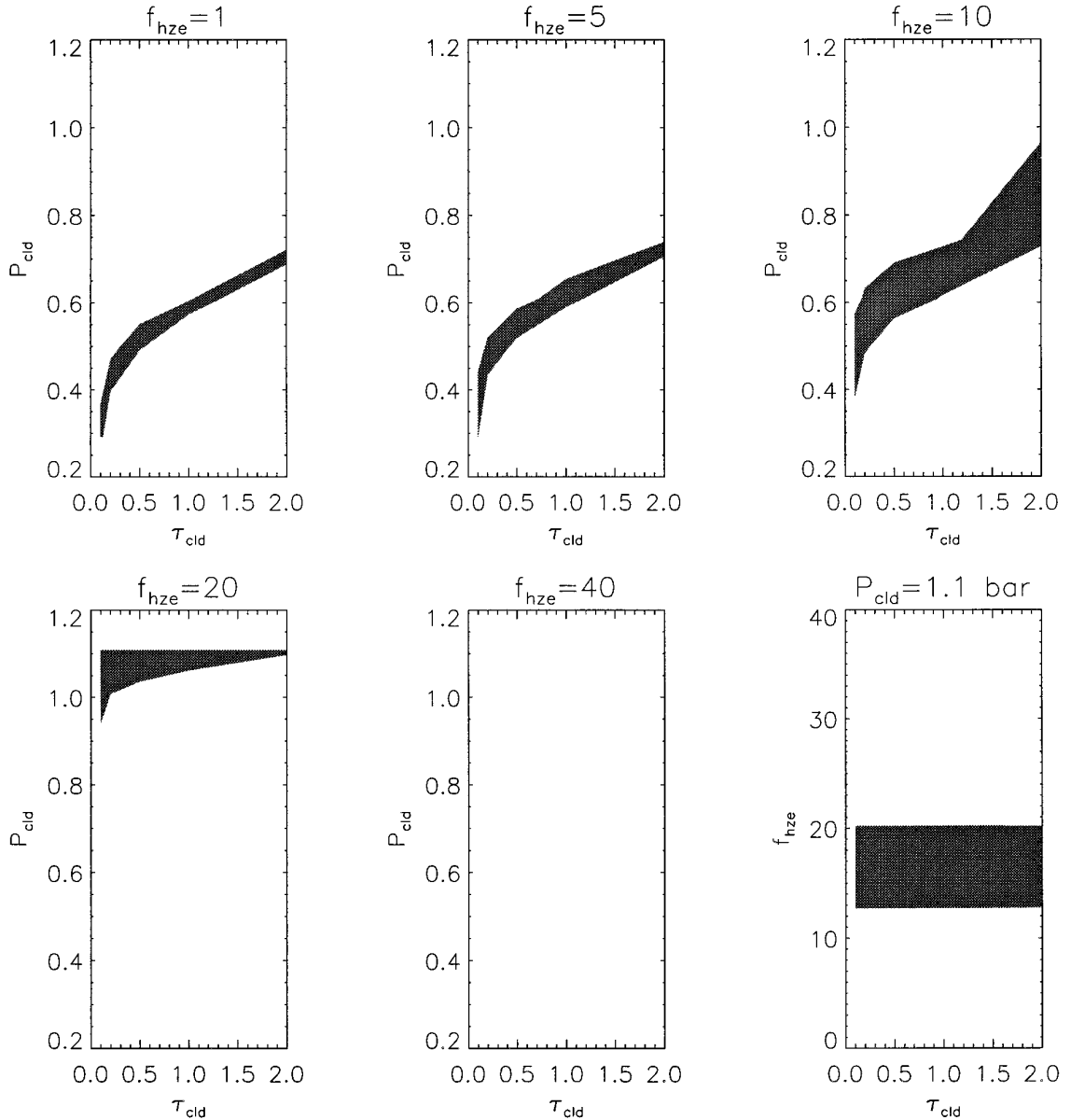


FIG. 9. 1996 1.99- μm results from varying the methane cloudtop pressure P_{cld} , the haze-column density scaling factor f_{hze} , and the cloud optical depth τ_{cld} . The bottom right panel shows the variation of f_{hze} vs τ_{cld} for a fixed cloud pressure level of 1.1 bar. The cloud optical depth is relatively insensitive to low haze column densities or cloudtop pressure for high haze column densities.

4.3. Troposphere

The two “continuum” filters (those with almost no molecular absorption) at 1.28 and 1.58 μm are insensitive to the location of the CH_4 cloud, as it attenuates incoming radiation by the same amount regardless of its location. Thus, the cloud cannot be resolved from the lower cloud at these wavelengths. These bandpasses proved to be insensitive to the amount of haze, which typically contributed an optical depth on the order of 10^{-4} per baseline haze-column density. The solution space of each bandpass is

similar, as can be seen in Fig. 10, where we compare the relation between the extinction of both clouds. At the nominal lower cloud top location of 3.0 bars and any location lower in the atmosphere, the relation is largely insensitive to the lower cloud, but as the cloud top is moved to 2.0 bar (Fig. 11) the sensitivity increases. Using the solution space created with a 3.0 bar lower cloudtop (Baines *et al.* 1995a), we see a linear relationship between the two cloud extinction opacities

$$\tau_{\text{cld}2} = -6\tau_{\text{cld}} + 15. \quad (4)$$

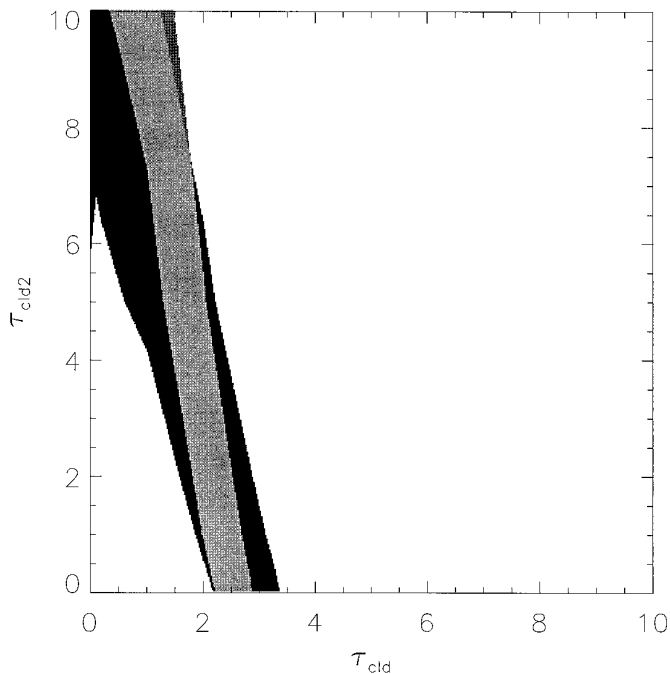


FIG. 10. The solution space for the 1.28- and 1.58- μm analysis for a haze-column density scaling factor f_{hze} of 20. The free parameters are the tropospheric cloud optical depths τ_{cld} and τ_{cld2} . Cloud locations are as shown in Fig. 3. As in Fig. 8, the lighter region represents the overlap of allowed solutions for both filters, with the 1.28- μm optical thicknesses being scaled using Mie theory to match those at 1.58 μm . The darkest region is the fit solely for 1.28 μm , while the medium shade is for 1.58 μm . For our nominal model we chose τ_{cld} of 1.5, τ_{cld2} of 6.0 as consistent with other results (Rages *et al.* 1991), however all solutions are equally valid.

If the optical depth in the 1–2- μm region can be established as being no more than 3 or 4, this would be a valuable tool in determining the size of the cloud particles, which are indistinguishably optically thick in the visible (Baines and Bergstralh 1986, Pollack *et al.* 1986, Trafton 1987, Doose *et al.* 1988, Baines *et al.* 1995a, Rages *et al.* 1991).

4.4. Model Comparison

In Table VII, we compare the parameters of our best atmosphere model with those of Rages *et al.* (1991) and Baines *et al.* (1995a). The geometric albedo spectra of our and the Baines *et al.* (1995a) models are shown in Fig. 13. Labeled optical depths of the CH_4 cloud are at 1.58 μm for our model, and at 0.7 μm for the other two. The Baines model does not use the Rages haze structure, but a similar model, also derived from Voyager results by Pollack *et al.* (1987) with nearly the same column density of suspended particles. As seen in Fig. 14, the extinction efficiency Q_{ext} for mean cloud particle sizes of 1 μm is greater at 1.58 μm than at 0.7 μm by approximately 20%, yielding an expected value for the total cloud optical depth of 1.6 at 1.58 μm

when compared to the model of Rages *et al.* (1991), within the errors of both models.

5. DISCUSSION

We have examined the properties of scatterers in the uranian atmosphere beyond 1 μm . Our results confirm the likely seasonal nature of the albedo as explored by Lockwood *et al.* (1983) and Hammel (1996). When Voyager encountered Uranus, the planet was at summer solstice, and the planet exhibited similar temperature profiles at both polar regions (Hanel *et al.* 1986). Ten years later, the southern hemisphere has experienced nearly 20 years of constant insolation, which could lead to an increase in polar haze formation. We show that the disk-averaged stratospheric haze-column density has indeed risen by a factor of 15 to 25 with a best fit of 20 for the solar-facing hemisphere in the intervening time. This interpretation of the increased scattering is not unique and could also be related to an increase in the mean modal radius of the particles. However, larger particles would fall more rapidly, leading to a decrease in the column density. In addition the effects of nonspherical particles have not been included, but these are not likely to be significant at the small size parameters considered in this work (Pollack and Cuzzi 1980). Thus, a number density change is the more likely explanation.

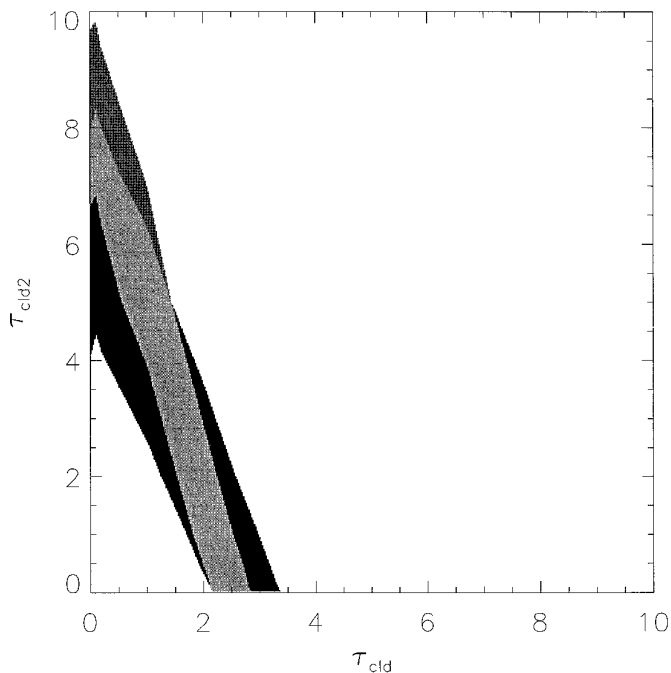


FIG. 11. The computation of Fig. 10 was repeated to examine the effect of moving the lower cloud top to 2.0 bars. All results with a cloudtop lower than 3.0 bars closely resemble Fig. 10.

TABLE VII
Model Parameters

Model	n_i	f_{hze}	$f_{\text{CH}_4, \text{s}}$	P_{cld}	τ_{cld}	$P_{\text{cld}2}$	$\tau_{\text{cld}2}$	$\bar{\omega}_{\text{cld}2}$
This work	5×10^{-3}	20	10^{-6}	1.1	1.3	2.5	6.0	0.99
Baines <i>et al.</i> (1995a)	0	≈ 1	10^{-6}	1.2	0.4	3.13	10	0.90
Rages <i>et al.</i> (1991)	$\sim 10^{-7}$	1	N/A	1.2	1.5	3.0	∞	0.65

There is no evidence for significant haze absorption at near-IR wavelengths, rather the haze particles scatter almost conservatively. This is not unexpected, as very few candidate molecules absorb between 0.5 and 3 μm . We are not highly sensitive to the stratospheric CH_4 abundance and show allowable mixing ratios only restricted by the upper limits of Orton *et al.* (1987) of 1×10^{-5} .

If there has indeed been a 20-fold increase in the haze-column number density in Uranus' atmosphere, it will warm the stratosphere. Marley and McKay (1997) found that while the haze described by Rages *et al.* (1991) did not play a substantial role in heating the stratosphere, haze abundances an order of magnitude larger could heat the 10 to 100 mbar region by over 10 K. Thus, new mid-infrared

observations of Uranus should show a warmer stratosphere than that seen in the Voyager epoch. Such observations would test the hypothesis that hazes play a significant role in the stratospheric energy balance (Appleby 1986).

In the troposphere, the CH_4 cloud has remained in the same location as in the Voyager epoch. If the mean particle sizes have remained constant near 1 μm , then it is likely that the column density of the cloud has remained the same as well. Properties of the lower tropospheric cloud are much more difficult to isolate, as they are dependent on our understanding of the upper cloud. If the lower cloud top has indeed risen above the 3.0 bar predicted by other works, then the cloud is likely to be less optically thick in the near-IR.

The asymmetry of CH_4 cloud as seen by Zellner *et al.*

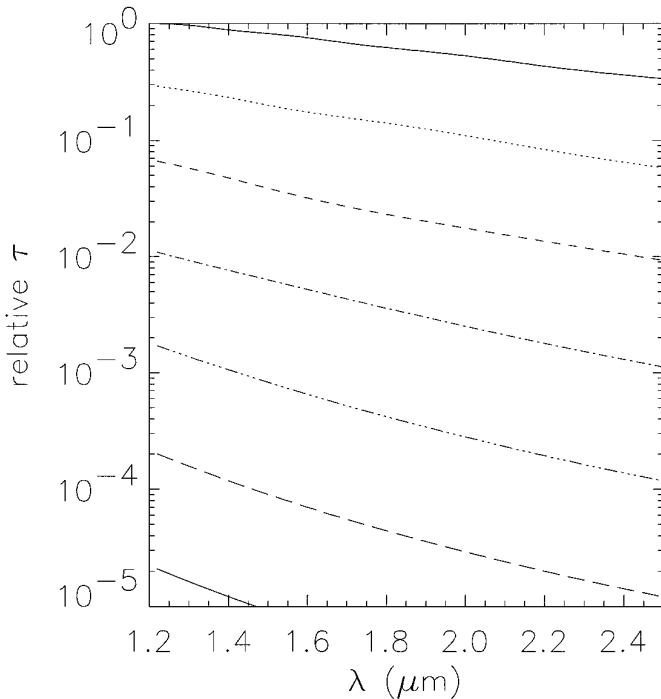


FIG. 12. The total extinction optical depth of atmospheric aerosols as a function of particle size and wavelength as computed from Mie theory using spherical particles. From the top, lines represent the results of $\log r = 0.00, -0.17, -0.33, -0.50, -0.67, -0.83,$ and -1.00 , where r is the particle radius measured in micrometers. The results are scaled to give a value of 1.0 for a 1- μm particle at 1.2 μm .

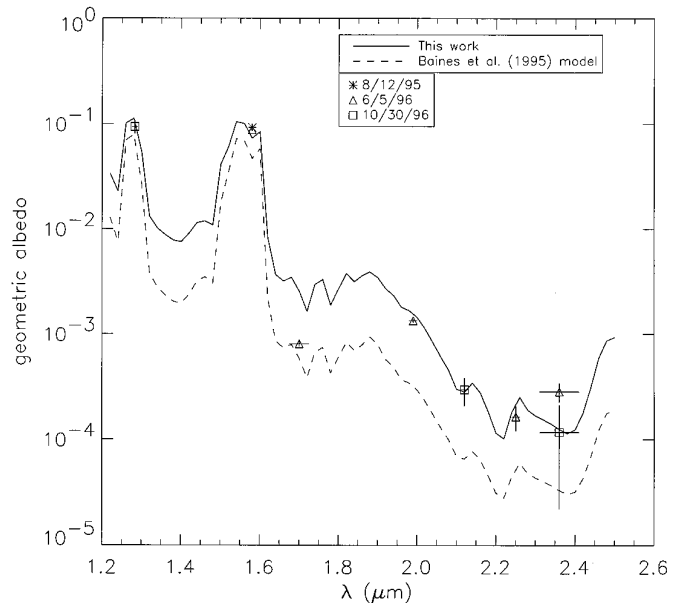


FIG. 13. The computed geometric albedos (taken every 0.02 μm) of three models of the uranian atmosphere in comparison with data taken on August 12, 1995, June 5, 1996, and October 30, 1996. Vertical error bars represent the photometric errors, and horizontal error bars (often smaller than the symbol) delimit the filter bandpasses. The nominal model employs the parameters described in Table VII as fit to the 1996 data set. The Baines *et al.* (1995a) model, derived from CH_4 and H_2 from 0.7 μm , is shown to be darker than observed when extrapolated into the near-IR.

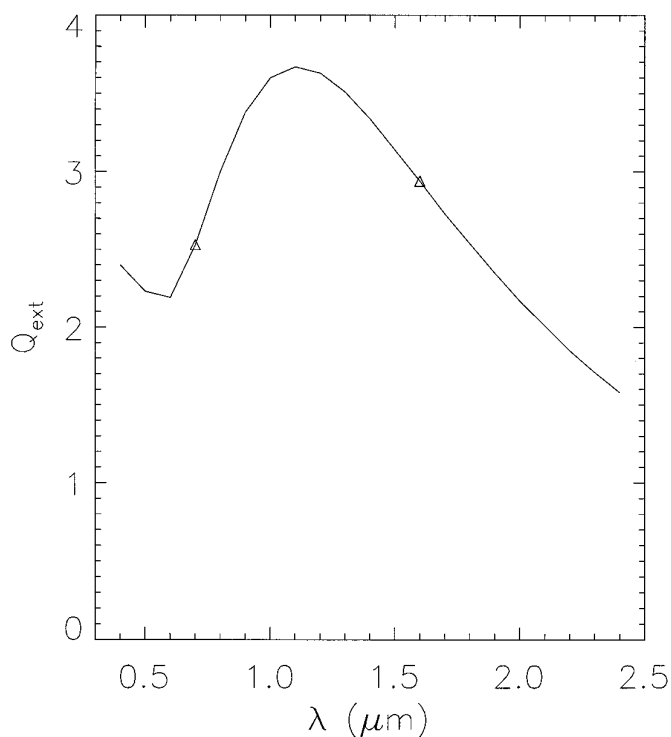


FIG. 14. Scattering efficiency Q_{ext} over the solar spectrum as computed using Mie theory with $1\text{-}\mu\text{m}$ spherical particles. The results at the comparison wavelengths for the optical and near-IR studies, $0.7\ \mu\text{m}$ and $1.58\ \mu\text{m}$ (triangles), are similar.

(1994) and other studies did not appear in our observations. This may be due to the high stratospheric haze abundance at the time of our observations. We will more thoroughly explore this problem with higher spatial resolution data in a future publication (Walter *et al.* 1997).

ACKNOWLEDGMENTS

We acknowledge the efforts of the staff at Apache Point Observatory in helping us acquire the data used in this study. This work was supported by NASA Grant NGT-51383, a Graduate Student Research Fellowship that funded one of us (CMW) through dissertation work, and NSF Grant AST-9624878.

REFERENCES

- Allen, C. W. 1973. *Astrophysical Quantities*, Athlone Press, London.
- Appleby, J. 1986. Radiative-convective equilibrium models of Uranus and Neptune. *Icarus* **65**, 383–405.
- Atreya, S. K., B. R. Sandel, and P. N. Romani 1991. Photochemistry and vertical mixing. In *Uranus* (J. T. Bergstralh, E. D. Miner, and M. S. Matthews, Eds.), pp. 110–146. Univ. of Arizona Press, Tucson.
- Baines, K. H. 1983. Interpretation of the $6818.9\ \text{\AA}$ feature observed on Jupiter, Saturn, and Uranus. *Icarus* **56**, 543–559.
- Baines, K. H., and J. T. Bergstralh 1986. The structure of the uranian atmosphere: Constraints from the geometric albedo spectrum and H_2 and CH_4 line profiles. *Icarus* **65**, 406–441.
- Baines, K. H., M. E. Mickelson, L. E. Larson, and D. W. Ferguson 1995a. The abundances of methane and ortho/para hydrogen on Uranus and Neptune: Implications of new laboratory $4\text{-}0\ \text{H}_2$ quadrupole line parameters. *Icarus* **114**, 328–340.
- Baines, K. H., R. A. West, L. P. Giver, and F. Moreno 1993. Quasi-random narrow-band model fits to near-infrared low-temperature laboratory methane spectra and derived exponential-sum absorption coefficients. *J. Geophys. Res.* **98**, 5517–5529.
- Baines, K. H., P. Yanamandra-Fisher, L. A. Lebofsky, T. W. Momary, and W. Golisch 1995b. High-spatial-resolution near-infrared absolute photometric imaging of the uranian and neptunian systems. *Bull. Am. Astron. Soc.* **27**, 1088.
- Binder, A. B., and D. W. McCarthy 1972. The infrared spectral albedo of Uranus. *Astrophys. J.* **171**, L1–L3.
- Birnbaum, G., A. Borysow, and G. Orton 1996. Collision-induced absorption of $\text{H}_2\text{-H}_2$ and $\text{H}_2\text{-He}$ in the rotational and fundamental bands for planetary applications. *Icarus* **123**, 4–22.
- Borysow, A. 1991. Modeling of collision-induced infrared absorption spectra of $\text{H}_2\text{-H}_2$ pairs in the fundamental band at temperatures from 20 to 300 K. *Icarus* **92**, 273–279.
- Borysow, A. 1992. New model of collision-induced infrared absorption spectra of $\text{H}_2\text{-He}$ pairs in the $2\text{-}2.5\ \mu\text{m}$ region at temperatures from 20 to 300 K: An update. *Icarus* **96**, 169–175.
- Borysow, A., and L. Frommhold 1989. Collision-induced infrared spectra of $\text{H}_2\text{-He}$ pairs at temperatures from 18 to 7000 K. II. Overtone and hot bands. *Astrophys. J.* **341**, 549–555.
- Borysow, A., L. Frommhold, and M. Moraldi 1989. Collision-induced infrared spectra of $\text{H}_2\text{-He}$ pairs involving $0 \leftrightarrow 1$ vibrational transitions and temperatures from 18 to 7000 K. *Astrophys. J.* **336**, 495–503.
- Brown, R. H. 1983. The uranian satellites and Hyperion—New spectrophotometry and compositional implications. *Icarus* **56**, 414–425.
- Brown, R. H., and D. P. Cruikshank 1983. The uranian satellites—Surface compositions and opposition brightness surges. *Icarus* **55**, 83–92.
- Conrath, B. J., D. Gautier, R. Hanel, G. Lindal, and A. Marten 1987. The helium abundance of Uranus from Voyager measurements. *J. Geophys. Res.* **92**, 15,003–15,010.
- Davies, M. E., V. K. Abalakin, M. Bursa, J. H. Lieske, B. Morando, D. Morrison, P. K. Seidelmann, A. T. Sinclair, B. Yallop, and Y. S. Tjuffin 1995. Report of the IAU/IAG/COSPAR working group on cartographic coordinates and rotational elements of the planets and satellites: 1994. *Celest. Mech. Dynam. Astron.* **63**, 127–148.
- de Pater, I., P. N. Romani, and S. K. Atreya 1991. Possible microwave absorption by H_2S gas in Uranus' and Neptune's atmospheres. *Icarus* **91**, 220–233.
- Doose, L. R., M. G. Tomasko, and A. M. Eibl 1988. The Uranus aerosol distribution at 10°S , 22°S , and 45°S latitude—Constraints from Voyager photometry and hydrogen quadrupole spectrophotometry. *Bull. Am. Astron. Soc.* **20**, 817.
- Elias, J. H., J. A. Frogel, K. Matthews, and G. Neugebauer 1982. Infrared standard stars. *Astron. J.* **87**, 1029–1034.
- Encrenaz, T., and T. Owen 1973. New observations of hydrogen quadrupole lines on Saturn and Uranus. *Astron. Astrophys.* **28**, 367–391.
- Fink, U., and H. P. Larson 1979. The infrared spectra of Uranus, Neptune, and Titan from 0.8 to 2.5 microns. *Astrophys. J.* **233**, 1021–1040.
- Gulkis, S., E. T. Olsen, M. J. Klein, and T. J. Thompson 1983. Uranus: Variability of the microwave spectrum. *Science* **221**, 453–455.
- Hammel, H. B. 1996. Visible and near-IR imaging of giant planets: Outer manifestations of deeper secrets. *Bull. Am. Astron. Soc.* **28**, 1056.
- Hanel, R. A., B. J. Conrath, F. M. Flasar, V. G. Kunde, W. Maguire, J. C. Pearl, J. A. Pirraglia, R. Samuelson, D. Cruikshank, D. Gautier,

- P. Gierasch, L. Horn, and P. Schulte 1986. Infrared observations of the uranian system. *Science* **233**, 70–74.
- Hansen, J. E., and L. D. Travis 1974. Light scattering in planetary atmospheres. *Space Sci. Rev.* **16**, 527–610.
- Herzberg, G. 1952. Spectroscopic evidence of molecular hydrogen in the atmospheres of Uranus and Neptune. *Astrophys. J.* **115**, 337–340.
- Kuiper, G. P. 1949. New absorptions in the uranian atmosphere. *Astrophys. J.* **109**, 540–541.
- Labs, D., and H. Neckel 1968. The radiation of the solar photosphere from 2000 Å to 100 μ. *Z. Astrophys.* **69**, 1–73.
- Lindal, G. F., J. R. Lyons, D. N. Sweetnam, V. R. Eshleman, D. P. Hinson, and G. L. Tyler 1987. The atmosphere of Uranus: Results of radio occultation measurements with Voyager 2. *J. Geophys. Res.* **92**, 14,987–15,001.
- Lockwood, G. W., B. L. Lutz, D. T. Thompson, and A. Warnock III 1983. The albedo of Uranus. *Astrophys. J.* **266**, 402–414.
- Marley, M. S., C. P. McKay, and J. B. Pollack 1997. Thermal structure of Uranus' atmosphere. *Icarus*, submitted.
- McKay, C. P., J. B. Pollack, and R. Courtin 1989. The thermal structure of Titan's atmosphere. *Icarus* **80**, 23–53.
- Nicholson, P. D., and T. J. Jones 1980. Two-micron spectrophotometry of Uranus and its rings. *Icarus* **42**, 54–67.
- Orton, G. S., D. K. Aitken, C. Smith, P. F. Roche, J. Caldwell, and R. Snyder 1987. The spectra of Uranus and Neptune at 8–14 and 17–23 μm. *Icarus* **70**, 1–12.
- Pearl, J., M. Ngoh, M. Ospina, and R. Khanna 1991. Optical constants of solid methane and ethane from 10,000 to 450 cm⁻¹. *J. Geophys. Res.* **96**, 17,477–17,482.
- Pollack, J. B., and J. N. Cuzzi 1980. Scattering by nonspherical particles of size comparable to a wavelength: A new semi-empirical theory and its application to tropospheric aerosols. *J. Atmos. Sci.* **37**, 868–881.
- Pollack, J. B., K. Rages, K. H. Baines, J. T. Bergstralh, D. Wenkert, and G. E. Danielson 1986. Estimates of the bolometric albedos and radiation balance of Uranus and Neptune. *Icarus* **65**, 442–466.
- Pollack, J. B., K. Rages, S. K. Pope, M. G. Tomasko, P. N. Romani, and S. K. Atreya 1987. Nature of the stratospheric haze on Uranus: Evidence for condensed hydrocarbons. *J. Geophys. Res.* **92**, 15,037–15,065.
- Prinn, R. G., and S. J. Lewis 1983. Uranus' atmosphere: Structure and composition. *Astrophys. J.* **179**, 333–343.
- Rages, K., J. B. Pollack, M. G. Tomasko, and L. R. Doose 1991. Properties of scatterers in the troposphere and lower stratosphere of Uranus based on Voyager imaging data. *Icarus* **89**, 359–376.
- Savage, B. D., and J. J. Caldwell 1974. Ultraviolet photometry from the Orbiting Astronomical Observatory. XIII. The albedos of Jupiter, Uranus, and Neptune. *Astrophys. J.* **187**, 197–208.
- Smith, W. H., W. Macy, and C. B. Pilcher 1980. Measurements of the H₂ 4–0 quadrupole bands of Uranus and Neptune. *Icarus* **43**, 153–160.
- Strong, K., F. W. Taylor, S. B. Calcutt, J. J. Remedios, and J. Ballard 1993. Spectral parameters of self- and hydrogen-broadened methane from 2000 to 9500 cm⁻¹ for remote sounding of the atmosphere of Jupiter. *J. Quant. Spectrosc. Radiat. Trans.* **50**, 363–429.
- Toon, O. B., C. P. McKay, T. P. Ackerman, and K. Santhanam 1989. Rapid calculation of radiative heating rates and photodissociation rates in inhomogeneous multiple scattering atmospheres. *J. Geophys. Res.* **94**, 16,287–16,301.
- Trafton, L. M. 1976. The aerosol distribution in Uranus' atmosphere: Interpretation of the hydrogen spectrum. *Astron. Astrophys.* **207**, 1007–1024.
- Trafton, L. M. 1987. Uranus' (3–0) H₂ quadrupole line profiles. *Icarus* **70**, 13–30.
- Trauger, J. T., and J. T. Bergstralh 1981. Asymmetrical profiles of the H₂ 4–0 quadrupole lines in the spectrum of Uranus. *Bull. Am. Astron. Soc.* **13**, 732.
- Veverka, J., P. Thomas, T. V. Johnson, D. Matson, and K. Hausen 1986. Surface physics. In *Satellites* (J. A. Burns and M. S. Matthews, Eds.), pp. 342–402. Univ. of Arizona Press, Tucson.
- Walter, C. M., and M. S. Marley 1995. Near-IR spatially-resolved observations of Uranus. *Bull. Am. Astron. Soc.* **27**, 1089.
- Walter, C. M., H. B. Hammel, and M. S. Marley 1997. A vertically and spatially-resolved model of the scatters in the uranian atmosphere. *Icarus*, submitted.
- Weidenschilling, S. J., and J. S. Lewis 1973. Atmospheric and cloud structures of the jovian planets. *Icarus* **20**, 465–476.
- Zellner, B., P. K. Seidelmann, D. Pascu, C. Kowal, E. Wells, and D. Currie 1994. Recovery of inner satellites of Uranus. *Bull. Am. Astron. Soc.* **26**, 1163.
- Zheng, C., and A. Borysow 1995. Modeling of collision-induced infrared absorption spectra of H₂–H₂ pairs in the first overtone band at temperatures from 20 to 500 K. *Icarus* **113**, 84–90.